J Appl Physiol 122: 1167–1178, 2017.
First published January 5, 2017; doi:10.1152/japplphysiol.00543.2016.

RESEARCH ARTICLE

Microscale distribution and dynamic surface tension of pulmonary surfactant normalize the recruitment of asymmetric bifurcating airways

Eiichiro Yamaguchi, Liam P. Nolan, and Donald P. Gaver III

Department of Biomedical Engineering, Tulane University, New Orleans, Louisiana

Submitted 17 June 2016; accepted in final form 4 January 2017

Yamaguchi E, Nolan LP, Gaver DP III. Microscale distribution and dynamic surface tension of pulmonary surfactant normalize the recruitment of asymmetric bifurcating airways. *J Appl Physiol* 122: 1167–1178, 2017. First published January 5, 2017; doi:10.1152/japplphysiol.00543.2016.—We investigate the influence of bifurcation geometry, asymmetry of daughter airways, surfactant distribution, and physicochemical properties on the uniformity of airway recruitment of asymmetric bifurcating airways. To do so, we developed microfluidic idealized in vitro models of bifurcating airways, through which we can independently evaluate the impact of carina location and daughter airway width and length. We explore the uniformity of recruitment and its relationship to the dynamic surface tension of the lining fluid and relate this behavior to the hydraulic (P_{Hyd}) and capillary (P_{Cap}) pressure drops. These studies demonstrate the extraordinary importance of P_{Cap} in stabilizing reopening, even in highly asymmetric systems. The dynamic surface tension of pulmonary surfactant is integral to this stability because it modulates P_{Cap} in a velocity-dependent manner. Furthermore, the surfactant distribution at the propagating interface can have a very large influence on recruitment stability by focusing surfactant preferentially to specific daughter airways. This implies that modification of the surfactant distribution through novel modes of ventilation could be useful in inducing uniformly recruited lungs, aiding in gas exchange, and reducing ventilator-induced lung injury.

NEW & NOTEWORTHY The dynamic surface tension of pulmonary surfactant is integral to the uniformity of asymmetric bifurcation airway recruitments because it modulates capillary pressure drop in a velocity-dependent manner. Also, the surfactant distribution at the propagating interface can have a very large influence on recruitment stability by focusing surfactant preferentially to specific daughter airways. This implies that modification of the surfactant distribution through novel modes of ventilation could be useful in inducing uniformly recruited lungs, reducing ventilator-induced lung injury.

ARDS; lung; respiratory airways; surfactant; VILI

A VISCOUS FLUID LINING LAYER containing pulmonary surfactant, which is produced by type II alveolar cells, protects pulmonary airways and alveoli. Surfactant reduces the surface tension dynamically, reduces the energy of breathing, and plays a role in host defense. Furthermore, surfactant biophysical properties protect airways and alveoli from surface-tension-induced liquid instabilities that can obstruct airways and impede gas exchange (8, 11, 16).

In disease states such as acute respiratory distress syndrome (ARDS), extreme pulmonary edema occurs, leading to flooding of the air spaces. Surfactant properties can become deranged because of infiltration of plasma proteins that competitively adsorb to the air-liquid interface (48). ARDS has a mortality of 30–40% (~75,000 US deaths annually) and arises from insults such as bacterial infection (sepsis), liquid aspiration, or noxious gas inhalation. A hallmark of ARDS is the presence of fluid-filled lungs with high-surface-tension interfaces. ARDS afflicts individuals in the prime of their life, and survivors may suffer from long-term neurological deficits, depression, and decreased quality of life (20). Furthermore, ICU length of stay correlates with decreased quality of life, so improved treatment can have a long-term impact on patients and their families (19).

While surfactant inactivation during ARDS and lung injury is significant, surfactant replacement therapies have generally not been clinically successful (42). Recent model studies suggest that while surfactant replacement therapy is effective in the neonatal lung, the same delivery technique in the adult lung leads to a poorly mixed, highly nonlinear distribution that could cause inadequate delivery (8). Therefore, to date there are no medical treatments for acute lung injury/ARDS other than supportive care revolving around mechanical ventilation. Unfortunately, mechanical ventilation can cause ventilation-induced lung injury (VILI) through mechanisms associated with volutrauma and atelectrauma (30, 33). Therefore, mechanical ventilation is a "double-edged sword" because it is necessary for recovery and yet can exacerbate lung damage. Our goal is to develop an understanding of the surfactant distribution behavior and biomechanical stimuli-response relationships associated with ventilation to provide guidance toward improved ventilation approaches that can reduce VILI.

A number of studies have investigated the biomechanical interactions leading to atelectrauma at the airway scale (12, 31) and at the cellular level (5, 7, 23, 25). Those studies focused on the pressures necessary to recruit individual airways, the mechanical stimuli created by recruitment, and the biological responses to those stimuli. Those studies indicate that the pressure gradient near the tip of the finger of air that removes the liquid obstruction provides the strongest correlation to the degree of epithelial damage and barrier function (14, 22, 24, 25). However, those studies investigated only individual airways and did not address the complex geometries associated in the lung.

The behavior of a bifurcating network is much more complex than that of individual airways and has important physiological implications. For example, nonuniform recruitment could result in large regional variations of ventilation. In turn, this can result in a "baby lung" scenario that results in volu-

Address for reprint requests and other correspondence: D. P. Gaver III, 500 Lindy Boggs Bldg., Dept. of Biomedical Engineering, Tulane Univ., New Orleans, LA 70118 (e-mail: dpg@tulane.edu).

trauma to those portions of the lung that are patent, while other regions remain atelectic. A full understanding of this type of interaction would require a multiscale model that links airway and alveolar fluid-structure behaviors that incorporate physicochemical interactions (2, 9, 17, 32, 36, 39).

Successful full-lung models will require an understanding of the interactions that occur in the region of a bifurcation and the relative responses of daughter airways. In a previous study (45), we initiated investigations of the recruitment of bifurcating airways, following prior studies by others (3). That study investigated the microfluidic behavior of reopening a simple symmetric Y-shape channel—this demonstrated pulmonary surfactant's unique ability to maintain nearly symmetric recruitment of daughter airways, which could improve the likelihood of uniform recruitment of a multigenerational bifurcated network and thus maximize the potential for global opening. Mathematical modeling provided insight that suggests that the dynamically altered pressure drop across the air-liquid interface of the propagating finger of air stabilized the uniform reopening of the nearly symmetric system. That analysis illustrated why simply lowering the surface tension was not sufficient for uniform recruitment; rather, a velocity-dependent surface tension provides a variable pressure drop that is instrumental in stabilizing the system.

The present study follows up on the investigation of nearly symmetric bifurcations with the goal of identifying how the carina geometry and daughter airway asymmetry interact with surfactant properties to influence the uniformity of recruitment. The goal of this study was to investigate how microscale features of the bifurcation in concert with surfactant properties and distribution can affect larger-scale recruitment phenomena. This, in turn, may lead to an understanding of how ventilation processes could be modified to improve ventilation homogeneity in the entire lung through a redistribution of surfactant near airway bifurcations that would encourage the simultaneous reopening of asymmetric obstructed daughter airways.

METHODS

Experimental Design Principles

Experiments were designed to discriminate between different mechanisms that can lead to, or ameliorate, nonuniform recruitment of bifurcating airways. These mechanisms are described in detail in Ref. 45 and synopsized here. We follow Refs. 13 and 34 to partition the bubble pressure drop along the fluid-occluded section of a daughter channel as consisting of three components (Fig. 1):

$$P_{Bubble} = P_{Cap} + P_{Hyd} + P_{End} \quad (1)$$

P_{Cap} is the pressure jump that exists over the air-liquid interface at the progressing bubble tip, which is related to the nonequilibrium normal stresses (law of Laplace) at low capillary number (Ca),

$$P_{Cap} \sim \frac{2\gamma}{R_{Interface}} \quad (2)$$

where $R_{Interface}$ is the interfacial radius of curvature. P_{Cap} can therefore be modulated by a change in $R_{Interface}$ or by physicochemical modifications of the surface tension, γ.

P_{Hyd} is the hydraulic pressure loss due to viscous flow downstream of the bifurcation, which is approximated by channel Poiseuille flow,

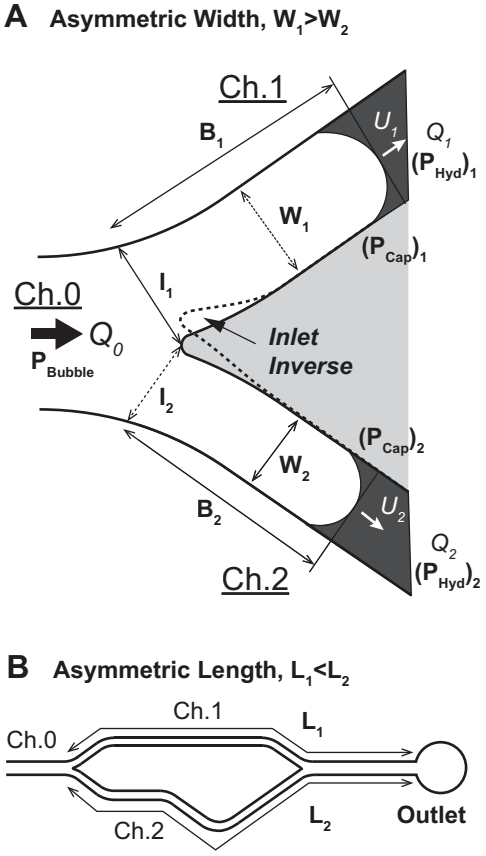

Fig. 1. Schematics of 3 patterns of asymmetric bifurcations. *A*: asymmetric width designs ($W_1>W_2$), with consistent inlet width (Inlet-Consistent = IC, $W_1/W_2 = I_1/I_2$), and with inverted inlet width (Inlet-Inverted = II, $W_1/W_2 = I_2/I_1$). *B*: Length-Asymmetric design. All designs share the same parent channel width, W_0 = 208 μm, sum of daughter section width, W_1+W_2 = 300 μm, and Ch.1 section length, L_1 = 4,800 μm.

$$P_{Hyd} \sim \frac{8\mu U}{R_{Hyd}^2} L(t) \quad (3)$$

where μ is viscosity, U is the velocity, R_{Hyd} is the hydraulic radius, and $L(t)$ is the length of the fluid-filled segment downstream of the air-liquid interface.

P_{End} is the pressure at the end reservoir. In our model system (see Fig. 1*A*), the daughter channels share a common end reservoir, the pressure at which can be defined as the reference pressure,

$$P_{End} = 0 \quad (4)$$

When the bubble splits to open the daughter channels (Ch.1 and Ch.2 in Fig. 1*B*), the pressure drop from the bubble to the end reservoir must balance. Therefore, the sum of the capillary and hydraulic pressure drops must be equivalent through Ch.1 and Ch.2:

$$(P_{Cap})_1 + (P_{Hyd})_1 = (P_{Cap})_2 + (P_{Hyd})_2 \quad (5)$$

So,

$$\left(\frac{2\gamma_1}{(R_{Interface})_1}\right) + \left(\frac{8\mu U_1(t) L_1(t)}{(R_{Hyd}^2)_1}\right) = \left(\frac{2\gamma_2}{(R_{Interface})_2}\right) + \left(\frac{8\mu U_2(t) L_2(t)}{(R_{Hyd}^2)_2}\right) \quad (6)$$

In our experimental models we perturb the geometry to investigate the effect of modification of the daughter channel widths (W_1

and W_2), which simultaneously influence the hydraulic radius given as $R_{Hyd} = WD/(W + D)$ in each of these branches. In addition, we perturb the inlet channel widths (I_1 and I_2), which modulates $R_{Interface}$ only at the entrance (a near-field effect). By methodically investigating the reopening behavior with these physical models using fluids of different physicochemical properties, we can satisfy our goal of identifying geometric and transport properties that influence the uniformity of airway reopening in branching networks.

Description of Asymmetric Bifurcation Microfluidic Device

All microfluid experimental devices were constructed with polydimethylsiloxane and a standard photolithography fabrication method (44). The interior of the flow chamber was treated with vinyl-terminated polydimethylsiloxane (DMS-V05, Gelelst) after exposure to oxygen plasma; this process sustains the hydrophilic surface properties throughout the duration of our experiments (38).

Each asymmetric model was created as a variation of the symmetric model shown in Fig. 1*A*, which is a two-dimensional version of idealized geometric properties of pulmonary bifurcations (29). We define the parent channel as *channel 0* (Ch.0) and the daughter channels as *channels 1* and *2* (Ch.1, Ch.2). The following properties exist in all models: *1*) the depth of all channels is uniform, $D = 150$ μm; *2*) the parent channel width is $W_0 = 208$ μm; *3*) the sum of the daughter channel widths is conserved, $W_1 + W_2 = 300$ μm; *4*) the daughter channels bifurcate at angle of 35° with initial branching curvature $R_{bi} = 525$ μm; *5)* the carina tip radius of curvature is $R_c = 75$ μm; *6*) each daughter links to outflow tubes ~700 μm from the bifurcation; and *7*) daughter branches are connected to a unified outlet downstream (2,400 μm from bifurcation) so as to apply a uniform downstream pressure.

The goal of this study was to identify the importance of geometric and physicochemical interactions and their effect on recruitment uniformity in asymmetric bifurcations. As such, we developed three distinct bifurcation variants to discriminate between capillary and hydraulic interactions that contribute to flow behavior. These variants are shown in Fig. 1, with specific dimensions listed in Table 1, and described below.

Width asymmetry with inlet consistent ($W_1/W_2)_{IC}$. In these models the daughter channels have asymmetric widths ($W_1 > W_2$) but symmetric lengths ($L_1 = L_2$). This design sets each entrance width to be equal to the related daughter channel width ($I_1 = W_1$, $I_2 = W_2$), hereafter referred to "Inlet-Consistent" and denoted by the subscript "IC." As described in *Experimental Design Principles*, this introduces an asymmetry of P_{Cap} both at the entrance and within the daughter branches. Furthermore, it introduces an asymmetry of P_{Hyd}. Without physicochemical interactions that cause dynamic surface tension, this asymmetry should lead to an initial preferential reopening of Ch.1 because it would have a lower P_{Cap}.

Length asymmetry (L_1/L_2). These devices are designed to have symmetric channel widths ($W_1 = W_2$) but asymmetric channel lengths ($L_1/L_2 = 0.974$) as shown in Fig. 1*B*. With this design, asymmetric flows are initiated solely by a differential in P_{Hyd}. Since $P_{Hyd} \sim L/R_{Hyd}^2$ this system has a hydraulic pressure ratio at the bifurcation entrance equal to $(P_{Hyd})_1/(P_{Hyd})_2 = L_1/L_2 = 0.974$. This hydraulic pressure ratio is equivalent to experiments with $(152/148)_{IC}$ apparatus. Since no differential in P_{Cap} exists, it is predicted that a significantly smaller degree of reopening asymmetry will exist in comparison to $(W_1/W_2)_{IC}$ experiments. Therefore, gradual increment of preferential opening of Ch.1 will be expected if no surfactant-induced physicochemical dynamic interactions on the moving bubble tip interface exist.

Width asymmetry with inlet inverted ($W_1/W_2)_{II}$. As with $(W_1/W_2)_{IC}$, the daughter channels have asymmetric widths ($W_1 > W_2$) and symmetric lengths ($L_1 = L_2$), but this design is used to evaluate the sensitivity of carina position by moving the carina tip (Fig. 1*A*, dotted line) so that the inlet width (I) is equal to the opposite daughter channel width ($I_1 = W_2$, $I_2 = W_1$), hereafter referred to "Inlet-Inverted" and denoted by the subscript "II." This design was chosen to highlight the inlet flow behavior, since the capillary

Table 1. *Descriptions of asymmetric Y channels and predicted/measured single-phase flow rates*

	Channel Design			Flow Rate Ratio (Q_1/Q_2)	
Name	Inlet ratio (I_1/I_2)	Daughter width ratio (W_1/W_2)	Length ratio (L_1/L_2)	Design	Measured
Small asymmetry					
a: $\left(\frac{152}{148}\right)$IC	152/148	152/148	1		1.04
b: $\left(\frac{152}{148}\right)$II	148/152	152/148	1	1.027	1.031
c: $\frac{L1}{L2} = 0.974$	150/150	150/150	0.974		1.03
Medium asymmetry					
a: $\left(\frac{155}{145}\right)$IC	155/145	155/145	1		1.121
b: $\left(\frac{155}{145}\right)$II	145/155	155/145	1	1.069	1.1
c: $\frac{L1}{L2} = 0.974$	150/150	150/150	0.935		1.1
Large asymmetry					
a: $\left(\frac{160}{140}\right)$IC	160/140	160/140	1		1.225
b: $\left(\frac{160}{140}\right)$II	140/160	160/140	1	1.143	1.193
c: $\frac{L1}{L2} = 0.974$	150/150	150/150	0.875		1.195

Width asymmetries are based on Ref. 27, which shows that 87% of bifurcations in respiratory zone have a diameter asymmetry ratio $D_1/D_2 < 1.15$ (major branch/minor branch) and >36% have $D_1/D_2 < 1.11$. Those asymmetries are in the range of those studied here [$W_1/W_2 = 160/140 = 1.14$; $W_1/W_2 = 152/148 = 1.03$].

Table 2. *Dynamic surface properties of test solutions*

	Concentration, mg/ml	γ_0, dyn/cm	γ_{min}, dyn/cm	γ_{max}, dyn/cm	$\Delta\gamma$, dyn/cm	$\Delta\gamma/\gamma_0$	β_{est}, dyn·s/cm^2
DPBS	0	65	65	65	0	0	0
SDS	1.73	33	30	34	4	0.12	80
001Infa	0.01	53	38	65	27	0.51	540
01Infa	0.1	31	10	65	55	1.77	1100
1.0Infa	1.0	24	5	35	30	1.25	600

γ_0, Static surface tension; $\Delta\gamma$, difference between the maximum (γ_{max}) and minimum (γ_{min}) dynamic surface tensions obtained from isotherm barrier close-open (1.0 mm/s) experiment at 37°C using mini-Langmuir trough. Solvent for all surfactant solutions is DPBS (containing 0.04 vol% of polystyrene fluorescent particles). SDS contains 1.73 mg/ml sodium dodecyl sulfate. 0.01Infa, 0.1Infa, and 1.0Infa contain 0.01, 0.1, and 1.0 mg/ml Infasurf, respectively.

pressure ratio is inverted from the capillary pressure ratio in the daughters, $[(P_{Cap})_1/(P_{Cap})_2]_{Inlet} = [(P_{Cap})_2/(P_{Cap})_1]_{Channel}$ and $[(P_{Cap})_1 > (P_{Cap})_2]_{Inlet}$ while maintaining $[(P_{Hyd})_1 < (P_{Hyd})_2]_{Channel}$ before the bubble bifurcation (see Table 1). So, under constant-surface tension conditions the inlet characteristics will cause an increased propensity for Ch.2 to begin opening preferentially, even though the daughter channel asymmetry is likely to result in long-range preferential flow in Ch. 1. Therefore comparison of the inlet behavior with various surfactant solutions will provide insight into the effect of nonuniform surfactant distribution on the air-liquid surface of the progressing bubble tip at the inlet region (45).

Test Solutions

Various test solutions were used to investigate the influence of physicochemical behavior on reopening uniformity. We chose these solutions on the basis of static and dynamic surface tension properties, as acquired by measurement with a barrier close/open five-cycle experiment using a Langmuir trough (KSV NIMA Biolin Scientific) with barrier speed of 1.0 mm/s at 37°C. The constant barrier speed is set to approximate average bubble speed in the bifurcation microfluid apparatus (see *Experimental Procedure*). The static surface tension, γ_0, was obtained from the measurement before the start of the isotherm barrier close/open experiment. $\Delta\gamma$ is reported as the difference of maximum and minimum surface tension in the last three cycles of oscillation.

Dulbecco's phosphate-buffered saline. Dulbecco's phosphate-buffered saline (DPBS) is a buffer solution and is used as the solvent phase for all surfactants in the experiment. This solution provides a constant surface tension $\gamma = 65$ dyn/cm under static and dynamic tests.

Sodium dodecyl sulfate solution. Sodium dodecyl sulfate (SDS) is an anionic surfactant with a high molecular diffusion rate near the air-liquid interface. The concentration (C = 1.73 mg/ml) is slightly below its critical micelle concentration. This solution reduces the surface tension to approximately $\gamma_0 = 30$ dyn/cm and has only a very small dynamic surface tension variation, $\Delta\gamma = 4$ dyn/cm.

Infasurf (0.01 mg/ml, 0.1 mg/ml, and 1.0 mg/ml). Infasurf (calfactant) (ONY) is an exogenous pulmonary surfactant analog used in surfactant replacement therapy. Concentrations are selected to investigate the importance of dynamic surface tension. With these concentrations, we found $\gamma_0 = 53$, 31, 24 dyn/cm and $\Delta\gamma = 27$, 55, and 30 dyn/cm for C = 0.01, 0.1, and 1.0 mg/ml, respectively. This suggests that different concentrations of Infasurf will display various degrees of sensitivity to the carina tip and channel asymmetries throughout the experiments.

Table 2 summarizes the static and dynamic surface properties of these test solutions obtained from a Langmuir trough/Wilhelmy plate (LTWP) surfactometer for DPBS and SDS and a pulsating bubble surfactometer for Infasurf, as described in DISCUSSION.

Image Acquisition

Particle image velocimetry (PIV) is well established and one of the most versatile tools to acquire whole field instantaneous flow fields under complex conditions (1). In past years, our laboratory has developed a microscale PIV (μ-PIV) system specialized for analysis of microscale interfacial flows during airway reopening (37, 46, 47). The modified μ-PIV system is depicted in Fig. 2*B*. Optics principles and system operation are unchanged from the system described in Yamaguchi et al. (45, 46). Volumetric illumination is provided by a dual-pulse Nd:YAG laser (λ = 532 nm, power = 15 mJ/pulse, duration = 4 ns; New Wave Laser Pulse Solo Mini, New Wave Research-ESI, Fremont, CA). The test solution is seeded by 1.0-μm fluorescent particles that have excitation/emission peaks at 535/575 nm to provide a return signal (λ = 550 nm) with minimal background noise. The PIV camera (PowerView Plus, TSI, Minneapolis, MN) CCD provides 2k × 2k effective pixel images with pixel resolution of 0.658 μm/pixel. In combination with a selected objective lens (×10/0.30 Plan Fluor, Nikon), the focal plane was set to the center of channel depth at ~15 μm. The camera and laser timing is controlled by a multichannel synchronizer and software (model 610035, TSI). The process control, image display, and postprocessing were coordinated by Insight 4G (TSI).

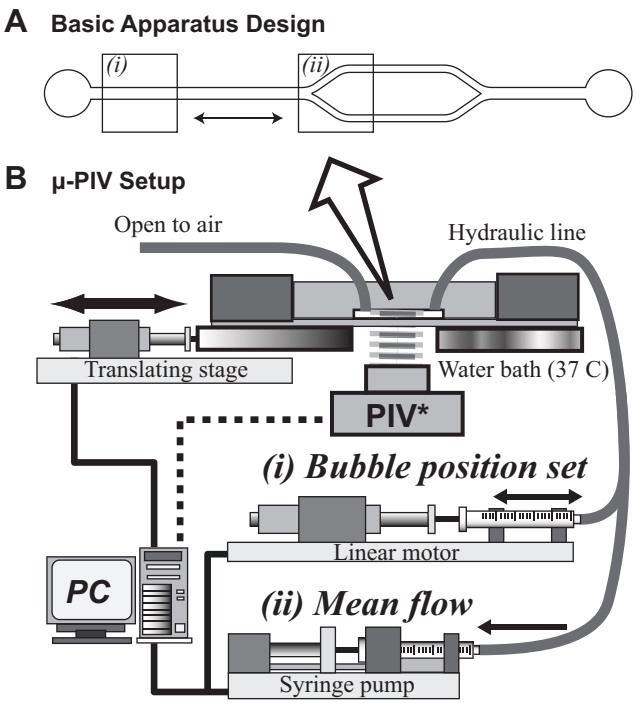

Fig. 2. Schematic of fluid apparatus basic design (*A*) and experimental setup (*B*). Linear motor with microsyringe (*i*) and the translating stage (37) are used to set initial bubble position in *frame i*, so that the observation window is moved to *frame ii*. Bubble progression and PIV image acquisition are controlled by PC-linked syringe pump (*ii*), CCD camera, and the pulsed laser system. *Detailed optical configuration of the PIV is available in Refs. 45 and 47.

All test solutions contained 0.04 vol% of 1.0-μm-diameter fluorescently dyed particles (Nile red, λ = 535/575 nm; Molecular Probes) in order to obtain fluorescent images with sufficient vector resolution for computing average flow rate of each channel instantaneously.

Experimental Procedure

The image acquisition observation window is adjusted to have the bifurcation carina at the left edge of each image (Fig. 2*A*, *frame ii*). With this orientation, we capture the image of the interface as it migrates through the system and observe the downstream liquid phase for interrogation of instantaneous flow velocity. The combination of computer-controlled linear actuator/syringe pumps (electromagnetic direct linear motor P01-23x80/30x90 and E200-AT, Linmot) and the motorized sliding stage allows us to set the initial bubble tip position ~10 mm upstream of the bifurcation point (Fig. 2*A*, *frame i*), before each run. The unified inlet (left reservoir in Fig. 2*A*) is open to the air, and the occluded fluid is drained from the unified outlet (right reservoir in Fig. 2*A*) at $Q = 1.17$ μl/min to achieve an average flow velocity in the parent channel of approximately $U = 0.5$ mm/s.

During each trial, image acquisition consists of 80 pairs of images at a rate of 7.25 pairs/s. The bubble tip appears after fully developed flow has commenced as shown in Fig. 3, after 4 s from the initiation of the flow. This provides a sufficient duration to capture the entire bubble bifurcation process and progression in daughter sections in the frame. Each experiment is completed $n = 5$ times for statistical analysis.

The interrogation of fluorescent images employs a recursive Nyquist grid with an FFT correlation engine and a Gaussian peak algorithm with a first 64 × 64-pixel interrogation window and a second smaller 32 × 32-pixel (with 50% overlap) interrogation window. An expected range of the progressing bubble speed in the daughter section is ~0–0.9 mm/s; therefore $\Delta t = 4.0$ ms is set as the time delay between each pair of fluorescent particle images in order to have a displacement of fewer than 8 pixels (25% of interrogation window size).

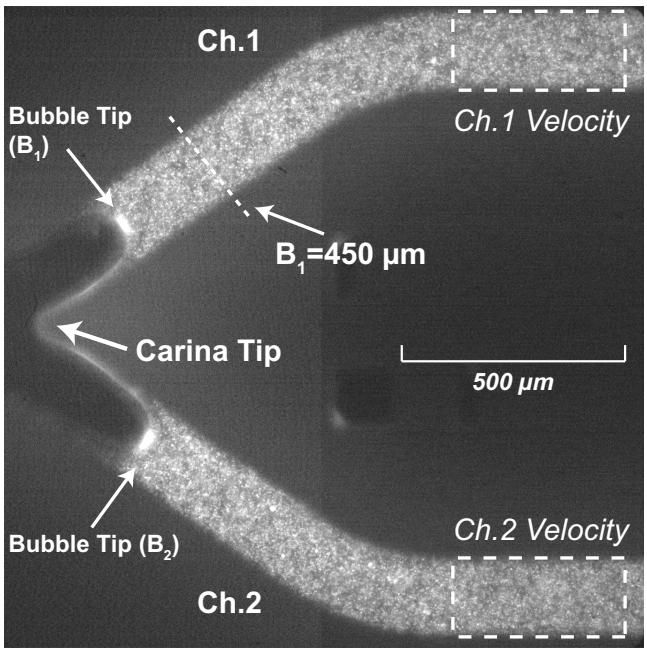

Fig. 3. Example of fluorescent particle image in the vicinity of a bifurcation. Bright region demonstrates the emission of high concentrations of fluorescent particles in the occluding liquid phase. Instantaneous bubble velocities and corresponding positions in daughter sections can be closely estimated from the PIV analysis in the dashed rectangular areas.

Data Processing

The present image acquisition system provides a pair of 2k × 2k pixel images with pixel resolution of 0.658 μm/pixel at 7.25 sets/s. Therefore each set of images can generate a 128 × 128 vector field with spatial resolution of 10.53 μm/vector at a temporal resolution of 7.25 frames/s. Since the daughter channel widths are ~150 μm, the observation frame provides ~14 vectors, which resolves sufficient detail to estimate velocity profile and maximum velocity at center line. Since the focal plane of the μ-PIV measurement is adjusted to the middle of the channel depth, the maximum velocity of the channel can be closely approximated and then converted to an average flow rate by using rectangular duct flow profiles, following Ref. 45. We define $t = 0$ as the moment when the progressing interface reaches the carina.

To assess reopening behavior, we monitor the instantaneous positions of the bubble tip positions downstream of the carina for each branch [$B_1(t)$, $B_2(t)$] in Fig. 1. To do so, we integrate the instantaneous flow velocity beginning from the time that the interface reaches the carina [$t = 0$ s; $B_1(0) = B_2(0) = 0$], and we use conservation of mass to predict the position by assuming that the residual film thickness is insignificant. Since the *Ca* for the system is very low ($\sim 10^{-6}$), this estimate of bubble position is accurate (6, 10, 18, 21, 43). Henceforth, we use the bubble position ratio, $B_1(t)/B_2(t)$, as the key parameter to quantify the reopening uniformity.

RESULTS

Design Validation

As described in *Description of the Asymmetric Bifurcation Microfluidic Device*, three distinct types of asymmetric models were fabricated: $(W_1/W_2)_{IC}$, (L_1/L_2), and $(W_1/W_2)_{II}$. To validate the accuracy of these designs, we measured the flow rate ratio Q_1/Q_2 for single-phase viscous flow through each branch. For example, the slightly asymmetric group, $(152/148)_{IC}$, $(152/148)_{II}$, and $L_1/L_2 = 0.974$, were designed to obtain the same hydrodynamic resistance and should therefore have an identical flow rate ratio, $Q_1/Q_2 = 1.027$. These flow rate ratios were evaluated experimentally with the μ-PIV system. The experimental data in Table 1 confirmed that we have fabricated asymmetry groups that provide three different distinctive degrees of asymmetry and that the variation in asymmetry between each subgroup is <3%.

Representative Responses of Asymmetric Systems

Representative data of experiments with constant surface tension (DPBS) and dynamic surface tension (0.1 mg/ml Infasurf) are presented in Fig. 4, with $t = 0$ defined as the instant when the bubble tip impinges the carina. These data represent the positions of $n = 5$ runs, and each data point has a 5–10% standard deviation (data not shown). The presented data sets are selected from the smallest degree of asymmetry [$(152/148)_{IC}$, $L_1/L_2 = 0.974$, and $(152/148)_{II}$], since the more highly asymmetric systems show less sensitive behavior to different test solutions. Furthermore, DPBS and C = 0.1 mg/ml Infasurf were selected to demonstrate the impact of physicochemical interactions on reopening asymmetry, since these responses bracket the behavior of other solutions.

As shown previously (45), the stabilizing effect of pulmonary surfactant is clearly visible in all asymmetric patterns. Overall, asymmetric designs $(W_1/W_2)_{IC}$ (*a*) and L_1/L_2 (*b*) demonstrate a consistent flow asymmetry that diverges flow to Ch.1, which has the lower resistance. As hypothesized above,

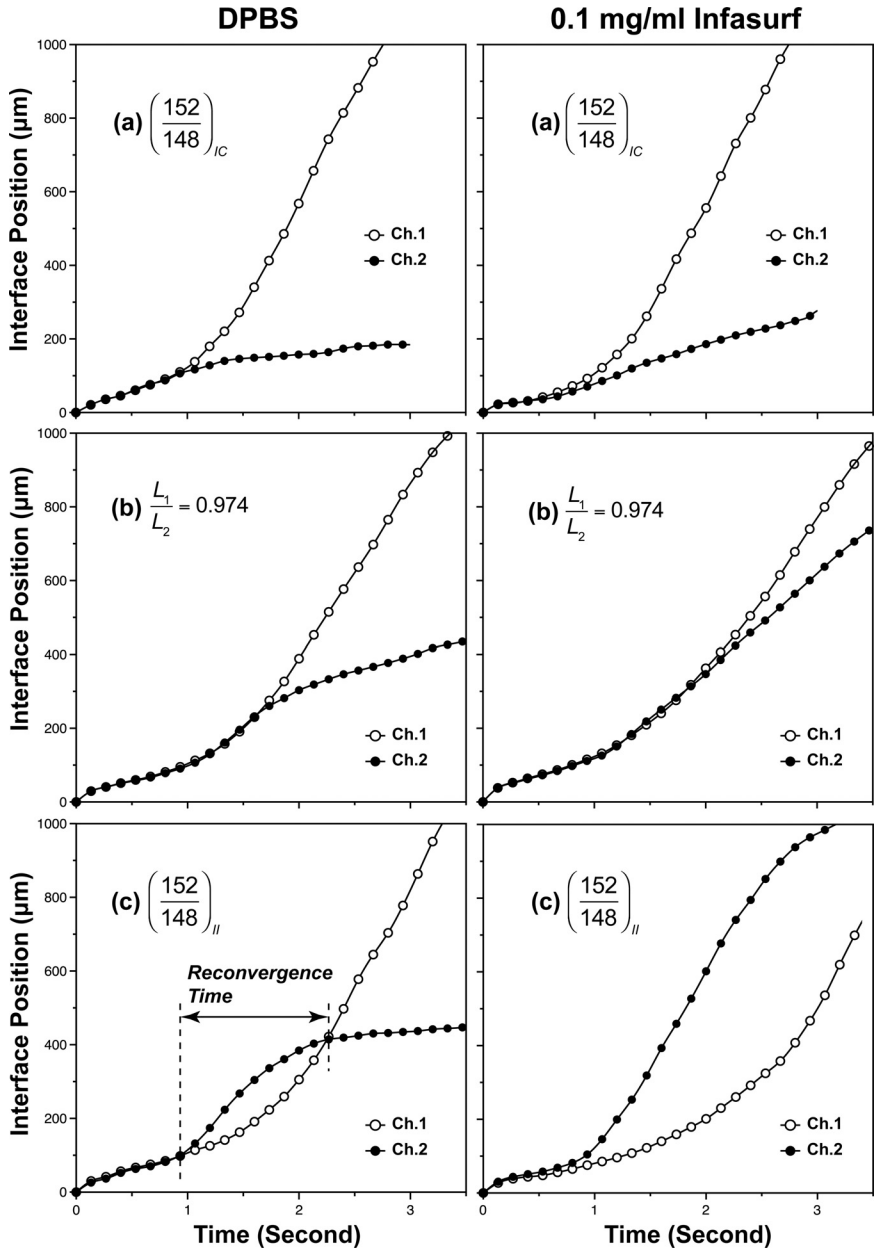

Fig. 4. Representative data set of airway reopening experiments under Inlet-Consistent (*a*); Length-Asymmetric (*b*), and Inlet-Inverted (*c*) conditions. Each data point represents the average of 5 trials.

modification of $(W_1/W_2)_{IC}$ causes a greater divergence to Ch.1 because modification of W simultaneously affects P_{Hyd} and P_{Cap}, while variation of L only affects P_{Hyd}.

To further decouple the effects of the capillary pressure drop from the hydraulic resistance, we include studies in which the inlet width ratio I_1/I_2 is inverted from the downstream width ratio W_1/W_2, as described above and denoted $(W_1/W_2)_{II}$. These experiments [(*c*), Fig. 4] demonstrate that the inlet effect on P_{Cap} induces Ch. 2 to reopen first, even though the overall hydraulic resistance in Ch. 1 is lower than that of Ch. 2 (as shown by the flow rate ratio in Table 1). Once Ch. 2 begins to reopen, however, the lower P_{Hyd} in Ch. 1 eventually leads the interface of Ch.1 to increase its relative velocity. The time at which the interfacial tip positions are equivalent ($B_1 = B_2$) is termed the "reconvergence time" (RT), and it is evident that physicochemical interactions induced by surfactant (C = 0.1 mg Infasurf) substantially increases RT. Below, we use RT as evidence of the nonuniform surfactant distribution along the interface near the progressing bubble tip, which affects reopening uniformity.

DISCUSSION

Figure 5 and Figure 6 present log-log plots of the reopening asymmetry behavior for $(W_1/W_2)_{IC}$ and L_1/L_2 experiments, respectively; the *x*-axis presents the interface position ratio B_1/B_2, and the *y*-axis presents the velocity ratio U_1/U_2 at the time when $B_1 = 450$ μm. Figures 5*A* and 6*A* represent the specific data, and Figs. 5*B* and 6*B* schematically illustrate the general trends. We chose the location $B_1 = 450$ μm because that represents the position that would correlate to the end of a generation following Wiebel and Gomez (40), which

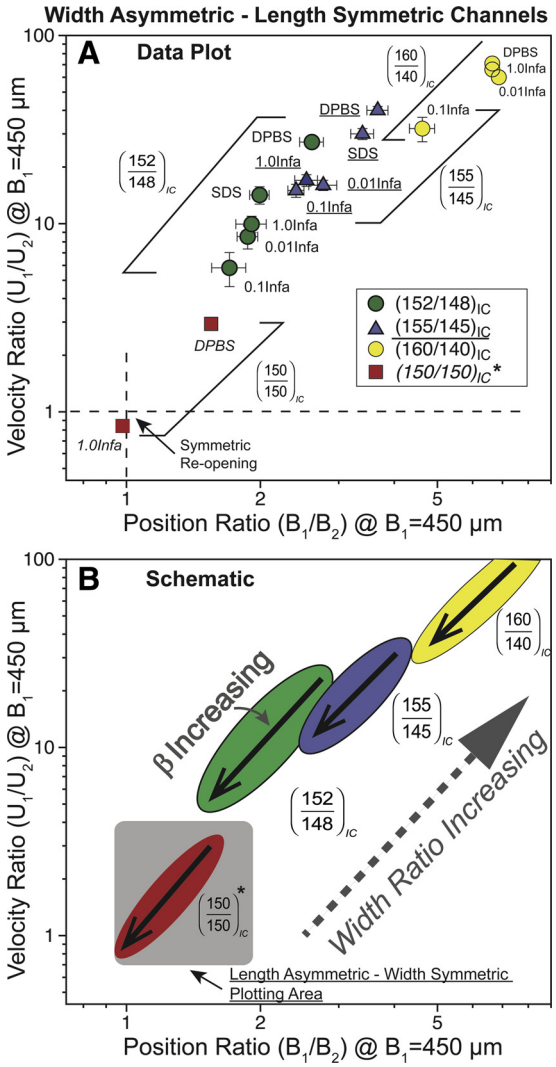

Fig. 5. Width-Asymmetric/Inlet-Consistent (IC) experiments. *A*: raw data. *B*: trend representation. *Data from Yamaguchi et al. (45).

describes the average length-to-diameter ratio of an airway in the respiratory zone as $L/D \sim 3$.

In Figs. 5 and 6, perfect reopening symmetry is represented by the point $B_1/B_2 = U_1/U_2 = 1$. If asymmetric reopening were consistent (i.e., a constant nonunity velocity ratio), then at any given time the data would exist at $B_1/B_2 = U_1/U_2$. Figure 5 demonstrates that symmetric reopening under $(W_1/W_2)_{IC}$ conditions does not occur and that in most cases $B_1/B_2 \ll U_1/U_2$, indicating that the reopening asymmetry increases rapidly. These trends are also evident in Fig. 6 (L_1/L_2 experiments), but the degree of reopening asymmetry is significantly smaller.

We can understand the asymmetric reopening behavior of Fig. 5 through $(W_1/W_2)_{IC}$ data (*a*) in Fig. 4. It is clear from the time-dependent behavior in Fig. 4 that two distinct regions exist. These consist of an initial region with simultaneous nearly symmetric motion, followed by an abrupt transition to asymmetry. The initial region is driven by a transitional increase in P_{Cap}, since R_{Cap} is reduced as the interface splits to enter into the daughter segments. This pressure increase requires a small time for the yield pressure to be reached, and the bubble progresses slowly to a position that is approximately one channel width downstream ($B \sim W$), with both daughter vessels reopening as the interfaces slowly creep at nearly the same speed. Subsequently, the reopening rates diverge substantially; Ch.1 accelerates quickly, while Ch.2 decelerates (especially with high constant surface tension, as with DPBS).

In contrast, for length-asymmetric channels [L_1/L_2 (*b*)] Fig. 4 and Fig. 6*A* show that the relative velocities are much smaller. In this case, Fig. 6*A* shows that the dynamic surface tension induced by Infasurf can cause nearly symmetric reopening to occur up to $B_1 = 450$ µm despite the fact that the apparatus has a clear channel length asymmetry.

The overall trends from of the $(W_1/W_2)_{IC}$ and (L_1/L_2) experiments are shown by schematic representations in Fig. 5*B* and Fig. 6*B*, respectively. Figure 5*B* shows that an increase in the width ratio substantially increases the asymmetry. For example, only a 15% differential in width, $(160/140)_{IC}$, results in a 100-fold change in relative velocity when a constant high-surface-tension fluid, DPBS, is used. However, the intro-

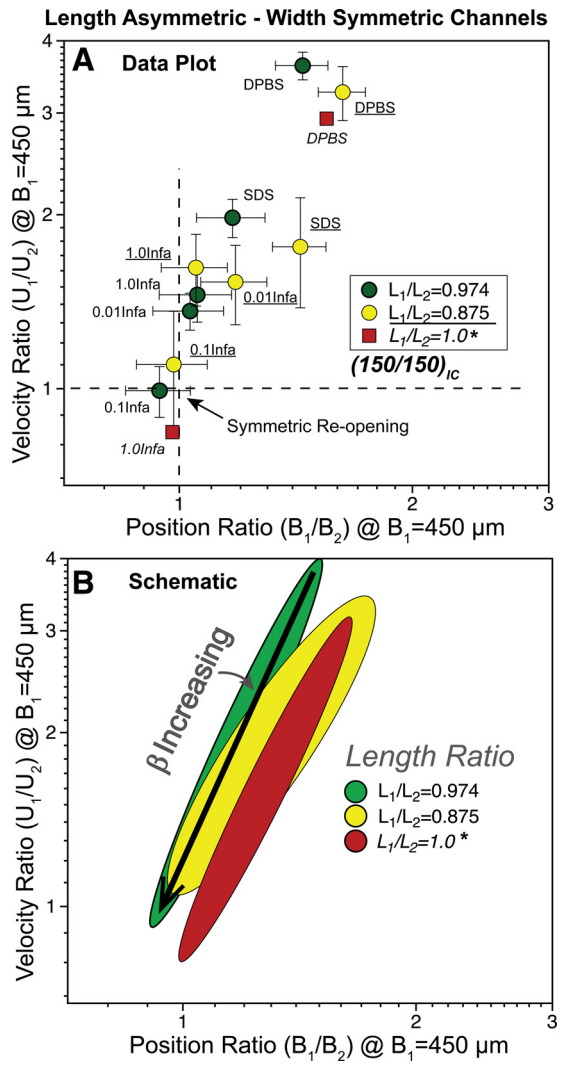

Fig. 6. Length-Asymmetric experiments. *A*: raw data. *B*: trend representation. Scale of velocity ratio is almost 10 times smaller than IC data (Fig. 5), even though initial flow rate ratios are nearly identical. *Data from Yamaguchi et al. (45).

duction of reduced static surface tension (SDS) or high dynamic surface tension ($\Delta\gamma/\gamma_0$) (0.01Infa, 0.1Infa, and 1.0Infa) substantially reduces the magnitude of asymmetric reopening. Figure 6*B* does not demonstrate as strong an influence of L_1/L_2 on reopening asymmetry, likely because it only explicitly modifies P_{Hyd}. However, decreasing the surface tension reduces the asymmetry, and this behavior is made more prominent with large dynamic surface tension, $\Delta\gamma/\gamma_0$.

The relative effects of P_{Cap} and P_{Hyd} can be understood from dimensional analysis for constant-surface tension fluids using *Eqs. 2 and 3*. Assuming a moderate surface tension $\gamma = 50$ mN/m (dyn/cm) and an obstruction fluid of viscosity equivalent to H_2O, the magnitude ratio of the two contributors to the pressure drop, P_{Cap}/P_{Hyd}, based on idealized geometric properties of respiratory airways (29), is $P_{Cap}/P_{Hyd} \sim O(10^2)$. The significantly larger impact of P_{Cap} in the present apparatus elucidates why the influence of width asymmetry is so much greater than that observed in length-asymmetric models. The magnitude of this effect is demonstrated by the gray-shaded region of Fig. 5*B*, which represents the entire domain of Fig. 6.

Importance of Dynamic Surface Tension

The relative importance of P_{Cap} helps to explain the extraordinary sensitivity of the system to dynamic surface tension. The variable surface tension modifies the relative surface tension ratio between Ch.1 and Ch.2 (γ_1/γ_2). This serves to equilibrate the hydraulic pressure drop in each segment by increasing the P_{Cap} in the branch that opens more quickly. To quantify this relationship, we hypothesized that a combination of sufficiently strong surface flow and slow sorption rates of the pulmonary surfactant generates an interfacial surfactant concentration difference between the daughter segments that increases the relative surface tension along the fast reopening branch in comparison to the slow branch (45). Therefore, by modulating the surface tension a differential in P_{Cap} is created between the branches. Since the total pressure drop is fixed (*Eq. 5*), this modifies the pressure available for flow, P_{Hyd}, which helps to equilibrate the bubble progression.

For example, consider the simple model of dynamic surface tension from (45),

$$\gamma_{eff} = f(\beta, U) \sim \gamma_0 + \beta U \tag{7}$$

where γ_0 is the equilibrium surface tension and β is inversely related to the rate of surfactant sorption at the surface—this is a measure of the deficiency of surfactant sorption to maintain a constant surface tension when an interface is not static. In that analysis, it was hypothesized that a large β could cause a differential surface tension between asymmetrically reopening daughter channels that helped to equilibrate reopening velocities.

To experimentally estimate this influence in our system, we used a LTWP system to evaluate the dynamic surface tension for DPBS and SDS. For Infasurf we measured the dynamic surface tension with a pulsating bubble surfactometer, since Infasurf produces low surface tension under high compression that can cause errors with a LTWP (28).

Specifically, we measured $\Delta\gamma = \gamma_{max} - \gamma_{min}$ as the maximum differential in the dynamic surface tension in hysteresis loop. For LTWP, we used a fixed barrier compression velocity, $U_{Compress} = 1$ mm/s, which is an order of magnitude estimate of the average surface expansion rate during the bubble penetration. For the pulsating bubble surfactometer our data are from an oscillation frequency f = 10 cpm, which provides an interface expansion rate of $U_{Compress} \sim 1$ mm/s.

$$\beta_{est} = \frac{\Delta\gamma}{U_{Compress}} \tag{8}$$

which is tabulated in Table 2.

Figure 5 and Figure 6 reveal the strong correlation between the increase of the dynamic surface tension parameter β and a reduction in the reopening asymmetry. For example, SDS has very low dynamic effects ($\beta = 20$ dyn·s/cm^2 and $\Delta\gamma/\gamma_0 = 0.12$) because it consists of small and highly mobile molecules that can adsorb rapidly to the developing interface. In contrast, Infasurf at C = 0.1 mg/ml (0.1Infa) has a much larger dynamic effect ($\beta = 115$ dyn·s/cm^2) with the greatest fractional change in surface tension ($\Delta\gamma/\gamma_0 = 0.74$). This occurs because of the low molecular mobility of the surfactant components that results in reduced diffusion and a slow adsorption rate that cannot adsorb rapidly enough to maintain a high surface concentration. In general, it is clear that a large dynamic surface tension is important for stabilizing the reopening velocities in daughter branches—this response may be of physiological importance for reducing regional ventilation heterogeneity.

Nonuniform Surfactant Distribution on the Surface and the Physicochemical Effect

The quantity and distribution of surfactant molecules that exist along the bubble tip interface are important factors to understand the physicochemical effect. Since dynamic surface tension results from the low mobility of pulmonary surfactant molecules and its relationship to velocity, a similar surfactant distribution will exist before the bifurcation point as it does afterward. Thus, the existence of the surfactant distribution should impact the initial stage of the bubble progress in the daughter airways, because it will set up the initial balance of γ_1 and γ_2 at inlets through setting the initial distribution of surfactant entering Ch.1 and Ch.2. Figure 7 provides a schematic of this concept. Here, the streamlines and location of a converging stagnation point illustrate the focusing of surfactant on the interface, which could impact the surfactant transport in the neighborhood of the bifurcation. Figure 7*A* provides experimentally obtained liquid phase streamlines from progressing infinite-long air bubble tip, with the converging stagnation point (black dot) accumulating surfactant at the center of the interface, as estimated from fluorescent microparticle imaging (47).

When a progressing bubble interface with a large-β surfactant solution is cleaved by the bifurcation carina, the surfactant accumulation at the converging stagnation point will be preferentially directed to the wider entrance, (see Fig. 7*B* for the Inlet-Consistent case). This causes the ratio $\Delta P_{Cap1}/\Delta P_{Cap2}$ to be reduced at the entrance in comparison to that of smaller-β surfactants because $\gamma_1 < \gamma_2$ and $R_1 > R_2$. Therefore Ch.1 reopens preferentially at the entrance, but the dynamic surfactant behavior modulates the reopening rate once the flow is developed.

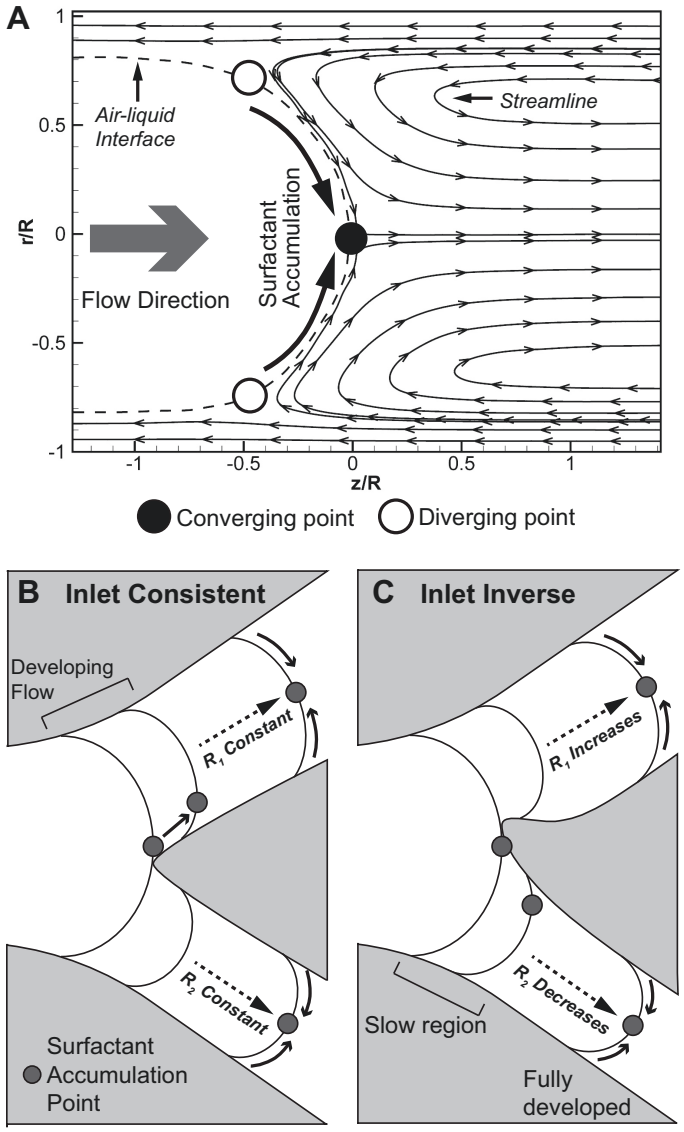

Fig. 7. *A*: schematic of experimentally obtained liquid-phase flow pattern near progressing air bubble tip in straight cylindrical channel (47). *B* and *C*: likely surface-phase surfactant transport during the interface migration near the bifurcation in an Inlet-Consistent bifurcation (*B*) and an Inlet-Inverted bifurcation (*C*).

In contrast, with the Inlet-Inverted case (see Fig. 7*C*), the converging stagnation point enters Ch.2 because its entrance region is wider, and this funnels the surfactant preferentially to the narrow channel. As the interface migrates into Ch.2, the narrowing entrance concentrates surfactant on the interface, which further reduces the surface tension in the narrower channel. The converse is also true—a reduced quantity of surfactant is convected to Ch.1, and the diverging width causes a relative increase in surface tension in the entrance region. To test this hypothesis, we developed Inlet-Inverted models (see Fig. 1*A*), in which the narrower daughter channel has an expanded entrance width equal to that of the wider channel's width, and vice versa. So, for example, as shown in Table 1, the channel $(155/145)_{II}$ has a width ratio of $W_1/W_2 = 155/145$ but an inlet ratio of $I_1/I_2 = 145/155$. Experiments using this Inlet-Inverted geometry were designed to obtain indirect evidence of the existence of the surfactant distribution and its effect on reopening symmetry.

The local effect of the entrance behavior on the Inlet-Inverted model (*c*) is shown in Fig. 4. With DPBS ($\beta = 0$ dyn·s/cm^2 and $\Delta\gamma/\gamma_0 = 0.12$) purely geometric issues are at play. Ch.2 initially reopens preferentially because the wider entrance results in $\Delta P_{Cap1} > \Delta P_{Cap2}$; however, after only 400 μm the Ch.1 bubble position takes a lead as $W_1 > W_2$ dominates the relationship. In Fig. 4, the impact that the inverted inlet poses on the bubble progress is denoted by the reconvergence time (RT).

With dynamic surface tension [Fig. 4; *c*, 0.1 mg/ml Infasurf], ΔP_{Cap} is reduced at the Ch.2 entrance by both geometric and physicochemical effects. Therefore, Ch.2 initially reopens preferentially and continues to reopen faster than Ch.1 far into the daughter channel despite the fact that the channel width ratio becomes $W_1 > W_2$. The increase of the RT indicates that the physicochemical interaction magnifies the difference between ΔP_{Cap1} and ΔP_{Cap2} at the entrance. Since all geometric features and flow rate balance before the bubble bifurcation are identical for two experiments in Fig. 4 (*c*), we conclude that the increase of the RT is caused by increased γ_1-to-γ_2 ratio at the entrance followed by the interfacial compression on Ch.2 (concentrating surfactant at the interface in a manner similar to that of a Langmuir trough) and expansion on Ch.1, which leads to surfactant enrichment in Ch. 2 and depletion in Ch. 1 until surfactant adsorption/desorption compensates.

Figure 8 presents the velocity ratio for Inlet-Inverted cases; in comparison to the data in Fig. 5 for Inlet-Consistent cases, it can be seen that far less reopening asymmetry exists (and in some cases it is reversed). Figure 9 elucidates the entrance effects by presenting RT vs. $\Delta\gamma/\gamma_0$ for $(152/148)_{II}$ experiments. In these experiments the difference in hydraulic diameter at the entrance is <3%; however, the RT increases by nearly threefold with an increase in dynamic surface as shown with 0.1Infa (C = 0.1 mg/ml Infasurf). The correlation of the increase of RT with $\Delta\gamma/\gamma_0$ indicates that the surface tension differential between Ch.1 and Ch.2 within the entrance region increases with the dynamic surface properties, which, as described above, is associated with an increased amount of accumulated surfactant preferential directed into Ch.2. This provides exper-

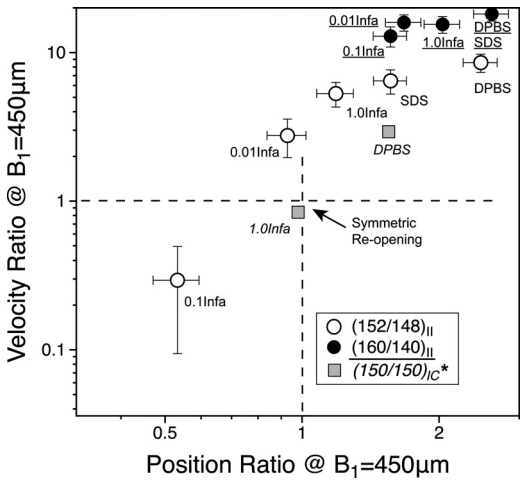

Fig. 8. Data from Width-Asymmetric/Inlet-Inverted (II) experiments. *Data from Yamaguchi et al. (45).

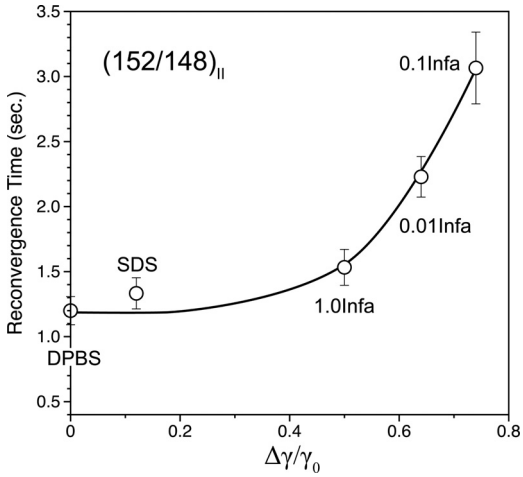

Fig. 9. Relationship between the dynamic surface tension property ($\Delta\gamma/\gamma_0$) and the reconvergence time in the Inlet-Inverted $(152/148)_{II}$ apparatus.

imental evidence of the existence of a nonuniform surfactant distribution along the interface front and the importance of dynamic surface properties of pulmonary surfactant, which was predicted in our previous work (45). It is also important to note that microscale entrance effects, such as small asymmetric placement bifurcation carina, can significantly affect global behavior of multichannel reopening because of the physicochemical interaction of pulmonary surfactant.

From this analysis, it is important to note that surfactant with a large β exists because of slow sorption properties that allow the creation of high-concentration regions due to convective focusing near converging stagnation points. However, these low sorption rates could lead to a high global surface tension, and this has been shown to lead to epithelial cell damage. Therefore, it is important to stabilize reopening uniformity while also reducing damage to the delicate tissue. For example, although the value of β is large for C = 0.01 mg/ml Infasurf, this concentration is not protective during steady-state reopening. In contrast, C = 1.0 mg/ml Infasurf has a higher sorption rate due to an increased concentration and has nearly the same value of β (see Table 2) but is highly protective (4, 25) because of a lower mean surface tension. Pulsatility may affect this optimization by inducing changes in the local concentration field.

Statistical Analysis

A paired *t*-test was conducted for statistical comparison across groups for the velocity and position ratios shown in Figs. 5 and 6. This analysis indicates that the results comparing surfactant (SDS or Infasurf) with surfactant-free (DPBS) solutions are statistically significant with $P \ll 0.001$ for all channels except $(160/140)_{IC}$. In that single case C = 0.1 mg/ml Infasurf provided results significantly different from DPBS ($P \ll 0.001$), while other concentrations of Infasurf showed less significance ($P < 0.1$) and SDS showed an insignificant difference. The lack of significance for SDS occurred because the yield pressure was not achieved, and the reduction of significance was a result of the lower values of β, which led to only slow motion in the narrow channel. Inlet-Inverted and Length-Asymmetric studies always demonstrated highly significant differences between surfactant and DPBS. This analysis shows that, in general, the dynamic surface tension properties afforded by Infasurf are important for inducing uniform airway recruitment in asymmetric bifurcations.

Limitations

This experimental in vitro study is intended to elucidate interfacial interactions that may influence the uniform recruitment of obstructed airways in the lung. However, this study has limitations that may reduce its direct applicability. Idealized microfluidic bifurcating channels were developed to investigate the importance of reopening geometry on the uniformity of airway recruitment in bifurcating systems, addressing fundamental principles associated with multiphase flows and the relationship between the capillary and viscous pressure drops. The use of bifurcation models with a rectangular cross section fulfilled this goal. While these structures permitted the careful examination of physical and physicochemical interactions, they did not investigate characteristics of more complex three-dimensional bifurcating geometries found in the lung. For example, we did not investigate the variation of the bifurcation angle that occurs during respiration or its orientation with respect to the gravitational vector.

In our studies we investigated the motion of long fluid-filled sections—it is likely that shorter plugs of liquid will obstruct the lung. This would introduce segments of trapped gas and multiple interfaces that could alter the system behavior. The structural compliance was also not investigated; clearly this would modify the geometry and interfacial instabilities based upon the local pressure (41). In reality, the terminal bronchioles and acini impose elastic resistance (P_{End}) that may act to balance the resistances and lead to symmetric reopening depending on the magnitudes of P_{Hyd} and P_{Cap}. In the present study, we purposely omitted the elastic resistance from the system to evaluate the influence of the branch-dependent ΔP_{Cap} accurately. These idealizations allow us to tease apart the physicochemical contributions that impact reopening at the microscale.

Also, the formalizations reduce the relevance to a true lung, where asymmetries may be time dependent and less subtle than those investigated in this study. Nevertheless, we explored the physical principles that can be exploited to develop a clinical approach. Further studies could investigate the sensitivity of our findings by introducing "noise" to the same structure or by introducing nonuniform forcing.

Additionally, the dynamic surface tension parameters β and $\Delta\gamma/\gamma_0$ were estimated from Langmuir trough and pulsating bubble experiments. While this analysis provides insight into the dynamic surface tension properties, the relationship between the interfacial and liquid phases in the surface tension experiments do not precisely model the transport processes in our bifurcation studies, and therefore the physicochemical models cannot entirely mimic the dynamics of the complex system. Despite this limitation, the parameters β and $\Delta\gamma/\gamma_0$ provide insight into the importance of dynamic surface tension in the uniformity of airway recruitment.

Conclusions

We have investigated the importance of dynamic surface tension in the uniformity of recruitment of idealized asymmetric pulmonary bifurcations. To complete this study, we isolated

the effects of capillary and viscous contributions to the reopening of airways branching from the bifurcation. This demonstrated that the surface tension difference between branches can substantially enhance recruitment uniformity in an asymmetric bifurcation, and that these surface-tension effects dominate viscous interactions. This reopening normalization occurs from two processes: *1*) a local change in the surfactant distribution at the entrance of the bifurcation that disproportionally cleaves surfactant and *2*) a velocity-dependent dynamic surface tension that occurs because of sorption rate limitations. We identified these processes by examining the sensitivity of recruitment uniformity to the placement of the carina and by variation of the downstream airway geometry. Through these studies we demonstrated that microscale effects in the region of the bifurcation have important implications that can sustain uniform reopening far into the daughter airways. Obviously, one cannot modify the precise configuration of an airway bifurcation geometry in real life. However, this study demonstrates that the surfactant concentration distribution can contribute substantially to uniform reopening. Our prior theoretical and experimental studies (15, 35) demonstrate that pulsatile flow may improve the distribution of surfactant through the use of a short retraction phase. The present study suggests that the local redistribution of surfactant may improve reopening uniformity while maintaining sufficient surfactant to decrease ΔP_{Cap} effectively, since flow reversal would cause the accumulating stagnation point to sweep from the tip toward the thin film (and back) during an oscillation phase. Currently we cannot set the phase a priori because of the geometric complexity of the lung; therefore variability, such as high-frequency and variable-frequency ventilation, may play an important role in providing conditions that could lead to homogeneous airway reopening. Further studies will investigate whether this flow reversal could prevent the preferential distribution of surfactant molecules and reduce the degree of sensitivity of the carina placement.

GRANTS

National Science Foundation Grant CBET-1033619 supported this study.

DISCLOSURES

No conflicts of interest, financial or otherwise, are declared by the author(s).

AUTHOR CONTRIBUTIONS

E.Y. and L.P.N. performed experiments; E.Y. and L.P.N. analyzed data; E.Y. interpreted results of experiments; E.Y. prepared figures; E.Y. and D.P.G. drafted manuscript; E.Y. and D.P.G. edited and revised manuscript; E.Y. and D.P.G. approved final version of manuscript.

REFERENCES

1. **Adrian RJ.** Twenty years of particle image velocimetry. *Exp Fluids* 39: 159–169, 2005. doi:10.1007/s00348-005-0991-7.
2. **Amin S, Majumdar A, Suki B.** Modeling the interaction of surfactant release and mechanical ventilation: reduction of lung injury with variable tidal volumes (Abstract). *Am J Respir Crit Care Med* 181: A1678, 2010. doi:10.1164/ajrccm-conference.2010.181.1_MeetingAbstracts.A1678.
3. **Baroud CN, Tsikata S, Heil M.** The propagation of low-viscosity fingers into fluid-filled branching networks. *J Fluid Mech* 546: 285–294, 2006. doi:10.1017/S0022112005007287.
4. **Bilek AM, Dee KC, Gaver DP III.** Mechanisms of surface-tension-induced epithelial cell damage in a model of pulmonary airway reopening. *J Appl Physiol (1985)* 94: 770–783, 2003. doi:10.1152/japplphysiol.00764.2002.
5. **Bilek AM, Dee KC, Gaver DP III.** Mechanisms of surface-tension-induced epithelial cell damage in a model of pulmonary airway reopening. *J Appl Physiol (1985)* 94: 770–783, 2003. doi:10.1152/japplphysiol.00764.2002.
6. **Bretherton FP.** The motion of long bubbles in tubes. *J Fluid Mech* 10: 166–188, 1961. doi:10.1017/S0022112061000160.
7. **Dailey HL, Yalcin HC, Ghadiali SN.** Fluid-structure modeling of flow-induced alveolar epithelial cell deformation. *J Comput Struc* 85: 1066–1071, 2007. doi:10.1016/j.compstruc.2006.11.012.
8. **Filoche M, Tai CF, Grotberg JB.** Three-dimensional model of surfactant replacement therapy. *Proc Natl Acad Sci USA* 112: 9287–9292, 2015. doi:10.1073/pnas.1504025112.
9. **Filoche M, Tai CF, Grotberg JB.** Three-dimensional model of surfactant replacement therapy. *Proc Natl Acad Sci USA* 112: 9287–9292, 2015. doi:10.1073/pnas.1504025112.
10. **Fuerstman MJ, Lai A, Thurlow ME, Shevkoplyas SS, Stone HA, Whitesides GM.** The pressure drop along rectangular microchannels containing bubbles. *Lab Chip* 7: 1479–1489, 2007. doi:10.1039/b706549c.
11. **Gaver DP III, Halpern D, Jensen OE.** Surfactant and airway liquid flows. In: *Molecular Mechanisms in Lung Surfactant (Dys)function*, edited by Nag K. New York: Dekker, 2005, p. 187–223.
12. **Gaver DP III, Samsel RW, Solway J.** Effects of surface tension and viscosity on airway reopening. *J Appl Physiol (1985)* 69: 74–85, 1990.
13. **Ghadiali SN, Gaver DP III.** An investigation of pulmonary surfactant physicochemical behavior under airway reopening conditions. *J Appl Physiol (1985)* 88: 493–506, 2000.
14. **Ghadiali S, Huang Y.** Role of airway recruitment and derecruitment in lung injury. *Crit Rev Biomed Eng* 39: 297–317, 2011. doi:10.1615/CritRevBiomedEng.v39.i4.40.
15. **Glindmeyer HW IV, Smith BJ, Gaver DP III.** In situ enhancement of pulmonary surfactant function using temporary flow reversal. *J Appl Physiol (1985)* 112: 149–158, 2012. doi:10.1152/japplphysiol.00643.2011.
16. **Grotberg JB, Jensen OE.** Biofluid mechanics in flexible tubes. *Annu Rev Fluid Mech* 36: 121–147, 2004. doi:10.1146/annurev.fluid.36.050802.121918.
17. **Hamlington KL, Ma B, Smith BJ, Bates JH.** Modeling the progression of epithelial leak caused by overdistension. *Cell Mol Bioeng* 9: 151–161, 2016. doi:10.1007/s12195-015-0426-3.
18. **Hazel AL, Heil M.** The steady propagation of a semi-infinite bubble into a tube of elliptical or rectangular cross-section. *J Fluid Mech* 470: 91–114, 2002. doi:10.1017/S0022112002001830.
19. **Hopkins RO, Weaver LK, Chan KJ, Orme JF Jr.** Quality of life, emotional, and cognitive function following acute respiratory distress syndrome. *J Int Neuropsychol Soc* 10: 1005–1017, 2004. doi:10.1017/S135561770410711X.
20. **Hopkins RO, Weaver LK, Collingridge D, Parkinson RB, Chan KJ, Orme JF Jr.** Two-year cognitive, emotional, and quality-of-life outcomes in acute respiratory distress syndrome. *Am J Respir Crit Care Med* 171: 340–347, 2005. doi:10.1164/rccm.200406-763OC.
21. **Huerre A, Miralles V, Jullien MC.** Bubbles and foams in microfluidics. *Soft Matter* 10: 6888–6902, 2014. doi:10.1039/C4SM00595C.
22. **Huh D, Fujioka H, Tung YC, Futai N, Paine R III, Grotberg JB, Takayama S.** Acoustically detectable cellular-level lung injury induced by fluid mechanical stresses in microfluidic airway systems. *Proc Natl Acad Sci USA* 104: 18886–18891, 2007. doi:10.1073/pnas.0610868104.
23. **Jacob AM, Gaver DP III.** Atelectrauma disrupts pulmonary epithelial barrier integrity and alters the distribution of tight junction proteins ZO-1 and claudin 4. *J Appl Physiol (1985)* 113: 1377–1387, 2012. doi:10.1152/japplphysiol.01432.2011.
24. **Jacob AM, Gaver DP III.** An investigation of the influence of cell topography on epithelial mechanical stresses during pulmonary airway reopening. *Phys Fluids (1994)* 17: 31502, 2005. doi:10.1063/1.1862642.
25. **Kay SS, Bilek AM, Dee KC, Gaver DP III.** Pressure gradient, not exposure duration, determines the extent of epithelial cell damage in a model of pulmonary airway reopening. *J Appl Physiol (1985)* 97: 269–276, 2004. doi:10.1152/japplphysiol.01288.2003.
27. **Koblinger L, Hofmann W.** Analysis of human lung morphometric data for stochastic aerosol deposition calculations. *Phys Med Biol* 30: 541–556, 1985. doi:10.1088/0031-9155/30/6/004.
28. **Krueger MA.** Evaluation of physicochemical properties of a pulmonary surfactant analogue. In: *Biomedical Engineering*. New Orleans, LA: Tulane University, 1999, p. 229.

29. **Lee D, Park SS, Ban-Weiss GA, Fanucchi MV, Plopper CG, Wexler AS.** Bifurcation model for characterization of pulmonary architecture. *Anat Rec (Hoboken)* 291: 379–389, 2008. doi:10.1002/ar.20643.
30. **Nieman GF, Gatto LA, Habashi NM.** Impact of mechanical ventilation on the pathophysiology of progressive acute lung injury. *J Appl Physiol (1985)* 119: 1245–1261, 2015. doi:10.1152/japplphysiol.00659.2015.
31. **Perun ML, Gaver DP III.** Interaction between airway lining fluid forces and parenchymal tethering during pulmonary airway reopening. *J Appl Physiol (1985)* 79: 1717–1728, 1995.
32. **Ryans J, Fujioka H, Halpern D, Gaver DP.** Reduced-dimension modeling approach for simulating recruitment/de-recruitment dynamics in the lung. *Ann Biomed Eng* 44: 3619–3631, 2016. doi:10.1007/s10439-016-1672-9.
33. **Slutsky AS, Imai Y.** Ventilator-induced lung injury, cytokines, PEEP, and mortality: implications for practice and for clinical trials. *Intensive Care Med* 29: 1218–1221, 2003. doi:10.1007/s00134-003-1793-0.
34. **Smith BJ, Gaver DP III.** Agent-based simulations of complex droplet pattern formation in a two-branch microfluidic network. *Lab Chip* 10: 303–312, 2010. doi:10.1039/B916380H.
35. **Smith BJ, Lukens S, Yamaguchi E, Gaver DP III.** Lagrangian transport properties of pulmonary interfacial flows. *J Fluid Mech* 705: 234–257, 2011. doi:10.1017/jfm.2011.391.
36. **Smith BJ, Lundblad LK, Kollisch-Singule M, Satalin J, Nieman G, Habashi N, Bates JH.** Predicting the response of the injured lung to the mechanical breath profile. *J Appl Physiol (1985)* 118: 932–940, 2015. doi:10.1152/japplphysiol.00902.2014.
37. **Smith BJ, Yamaguchi E, Gaver DP III.** A translating stage system for μ-PIV measurements surrounding the tip of a migrating semi-infinite bubble. *Meas Sci Technol* 21: 15401, 2010. doi:10.1088/0957-0233/21/1/015401.
38. **Sui G, Wang J, Lee CC, Lu W, Lee SP, Leyton JV, Wu AM, Tseng HR.** Solution-phase surface modification in intact poly(dimethylsiloxane) microfluidic channels. *Anal Chem* 78: 5543–5551, 2006. doi:10.1021/ac060605z.
39. **Suki B, Barabási AL, Hantos Z, Peták F, Stanley HE.** Avalanches and power-law behaviour in lung inflation. *Nature* 368: 615–618, 1994. doi:10.1038/368615a0.
40. **Weibel ER, Gomez DM.** Architecture of the human lung. Use of quantitative methods establishes fundamental relations between size and number of lung structures. *Science* 137: 577–585, 1962. doi:10.1126/science.137.3530.577.
41. **Whang J, Faulman C, Itin TA, Gaver DP III.** The influence of tethering and gravity on the stability of compliant liquid-lined airways. *J Biomech* 50: 228–233, 2017. doi:10.1016/j.jbiomech.2016.11.030.
42. **Willson DF, Truwit JD, Conaway MR, Traul CS, Egan EE.** The adult calfactant in acute respiratory distress syndrome trial. *Chest* 148: 356–364, 2015. doi:10.1378/chest.14-1139.
43. **Wong H, Radke CJ, Morris S.** The motion of long bubbles in polygonal capillaries. Part 1. Thin films. *J Fluid Mech* 292: 71–94, 1995. doi:10.1017/S0022112095001443.
44. **Xia Y, Whitesides GM.** Soft lithography. *Annu Rev Mater Sci* 28: 153–184, 1998. doi:10.1146/annurev.matsci.28.1.153.
45. **Yamaguchi E, Giannetti MJ, Van Houten MJ, Forouzan O, Shevkoplyas SS, Gaver DP III.** The unusual symmetric reopening effect induced by pulmonary surfactant. *J Appl Physiol (1985)* 116: 635–644, 2014. doi:10.1152/japplphysiol.00814.2013.
46. **Yamaguchi E, Smith BJ, and Gaver DP III.** μ-PIV for the analysis of flow fields near a propagating air-liquid interface. In: *The Particle Image Velocimetry— Characteristics, Limits and Possible Applications*, edited by Cavazzini G. Rijeka, Croatia: InTech, 2012, p. 261–281.
47. **Yamaguchi E, Smith BJ, Gaver DP III.** μ-PIV measurements of the ensemble flow fields surrounding a migrating semi-infinite bubble. *Exp Fluids* 47: 309–320, 2009. doi:10.1007/s00348-009-0662-1.
48. **Zasadzinski JA, Stenger PC, Shieh I, Dhar P.** Overcoming rapid inactivation of lung surfactant: analogies between competitive adsorption and colloid stability. *Biochim Biophys Acta* 1798: 801–828, 2010. doi:10.1016/j.bbamem.2009.12.010.